Journal of Biomedical Optics

SPIEDigitalLibrary.org/jbo

Spatial cluster analysis of nanoscopically mapped serotonin receptors for classification of fixed brain tissue

Michael Sams
Rene Silye
Janett Göhring
Leila Muresan
Kurt Schilcher
Jaroslaw Jacak

SPIE

Spatial cluster analysis of nanoscopically mapped serotonin receptors for classification of fixed brain tissue

Michael Sams,[a] Rene Silye,[b] Janett Göhring,[c] Leila Muresan,[d] Kurt Schilcher,[a] and Jaroslaw Jacak[a,e]
[a]Upper Austria University of Applied Sciences, Campus Linz, Garnisonstrasse 21, 4020 Linz, Austria
[b]Nerve Clinic Linz, Department of Pathology and Neuropatholgy, Wagner-Jauregg Weg 15, 4020 Linz, Austria
[c]Medical University of Vienna, Max F. Perutz Laboratories, Dr. Bohrgasse 9/3, 1030 Vienna, Austria
[d]Ecole Normale Supérieure, Department of Biologie, 46 rue d'Ulm, 75005 Paris, France
[e]Johannes Kepler University Linz, Altenbergerstrasse 69, 4040 Linz, Austria

Abstract. We present a cluster spatial analysis method using nanoscopic dSTORM images to determine changes in protein cluster distributions within brain tissue. Such methods are suitable to investigate human brain tissue and will help to achieve a deeper understanding of brain disease along with aiding drug development. Human brain tissue samples are usually treated postmortem via standard fixation protocols, which are established in clinical laboratories. Therefore, our localization microscopy-based method was adapted to characterize protein density and protein cluster localization in samples fixed using different protocols followed by common fluorescent immunohistochemistry techniques. The localization microscopy allows nanoscopic mapping of serotonin 5-HT_{1A} receptor groups within a two-dimensional image of a brain tissue slice. These nanoscopically mapped proteins can be confined to clusters by applying the proposed statistical spatial analysis. Selected features of such clusters were subsequently used to characterize and classify the tissue. Samples were obtained from different types of patients, fixed with different preparation methods, and finally stored in a human tissue bank. To verify the proposed method, samples of a cryopreserved healthy brain have been compared with epitope-retrieved and paraffin-fixed tissues. Furthermore, samples of healthy brain tissues were compared with data obtained from patients suffering from mental illnesses (e.g., major depressive disorder). Our work demonstrates the applicability of localization microscopy and image analysis methods for comparison and classification of human brain tissues at a nanoscopic level. Furthermore, the presented workflow marks a unique technological advance in the characterization of protein distributions in brain tissue sections. [DOI: 10.1117/1.JBO.19.1.011021]

Keywords: localization microscopy; cluster analysis; protein clusters; spatial analysis; fluorescent brain imaging; serotonin receptor.

Paper 130168SSRR received Mar. 27, 2013; revised manuscript received Sep. 19, 2013; accepted for publication Oct. 14, 2013; published online Dec. 2, 2013.

1 Introduction

Recent developments in fluorescence microscopy methods allow for the localization of single molecules with subdiffraction precision. Current nanoscopic imaging techniques are essentially based around two major concepts: stochastic single molecule localization and deterministic ensemble imaging. The best known examples of deterministic imaging techniques include stimulated emission depletion and structured illumination microscopy.[1–5] In contrast, stochastic super-resolution imaging techniques rely on precise positional determination of single molecules and image reconstruction. These techniques include, for example, photo-activated localization microscopy and stochastic optical reconstruction microscopy.[6–11] One application for super-resolution microscopy is the accurate determination of a protein's spatial and temporal cellular distributions. Apart from localization, these techniques also provide additional information about protein cluster characteristics (e.g., number of molecules per cluster and density), which are not available when imaged with conventional diffraction-limited optics.[12,13] Recently, the mentioned techniques were adapted for imaging human tissues.[14–16] In our study, we applied STORM microscopy on healthy and pathological brain tissue samples obtained postmortem to analyze the spatial distribution of receptors on neuronal and glial cells.

The STORM method is based on photo-activation of fluorescent molecules. However, in our experiments, we apply a modification of STORM called dSTORM (direct STORM). In the dSTORM technique, fluorophores switch between a detectable fluorescent and a nonfluorescent (dark) state by a light-induced chemical reaction.[11,17,18] This process is repeated many times and allows the reconstruction of an image via the molecular distribution within a sample. Especially in the case of the complex-organized brain, the precise characterization of receptor distribution will provide insights in brain tissue organization, as a tool to discriminate receptors on neuronal and glial cells, and finally in classification of brain's diseases. In order to test the model system, we have focused on nanoscopic localization of the well-characterized serotonin receptor 5-HT_{1A}, a G-protein-coupled receptor widely distributed in regions of frontal cortex, septum, amygdale, hippocampus, and hypothalamus. Interestingly, serotonin responses strongly correlate with depressive symptoms [major depressive disorder (MDD)], exhibiting low brain 5-HT abundance and reduced density of serotonin 1A receptor (5-HT_{1A}) and transporter (5-HTT).[19–22]

In this primarily technical study, we developed a statistical spatial analysis method for characterization of dSTORM

Address all correspondence to: Jaroslaw Jacak, Upper Austria University of Applied Sciences, Campus Linz, Garnisonstrasse 21, 4020 Linz, Austria. Tel: +43 699 11171075; E-mail: jaroslaw.jacak@jku.at

images tested on serotonin 5-HT_{1A} receptors in brain tissue samples using fluorescently labeled antibodies. The immunocytochemical approach allows nanoscopic two-dimensional (2-D) mapping of serotonin receptor groups. To enable anatomical orientation within the tissue of the frontal cortex, glial cells are also labeled with a second anti-glial fibrillary acidic protein (GFAP) antibody.

For proper comparison of image samples, we used our novel clustering-based analysis method at the single-molecule level. This analysis uses hierarchical clustering to construct molecule clusters with a given distance (size) between the molecule positions. For each prepared cluster set, a number of selected cluster features are calculated including shape, relative molecule density, relative number of fluorophores, and the distance of a cluster to the skeleton representation of a bulky fluorescent structure (e.g., glial cells). These empirical distributions of features form the basis of comparison in spatial patterns determined from the fluorescent two-color images.

To verify our method, healthy brain tissue (cryopreserved samples) were compared with epitope-retrieved and paraffin-fixed tissues, which was stored for different time periods. The comparison demonstrates the influence of long-term sample preservation, which is an important issue for further studies on bank material; So far, fixation artifacts have never been quantified on a nanoscopic level. Moreover, results on cluster densities, fluorophore numbers, shapes, and cluster distances-to-skeleton (representation of glia cells) determined from healthy brain tissues were compared with data obtained from brain samples of depressive patients.

The experimental results indicate that our method can be used for further studies on complex processes like receptor density changes. Furthermore, it allows tissue classification at a nanoscopic level of routine pathology samples of various diseases. Moreover, the presented relationship between the clusters and the structure of the bulk fluorescence image enables a more precise analysis of the concentration and the density of receptors surrounding the glia scaffold.

2 Materials and Methods

2.1 *Sample Preparation*

The tests of the platform were performed on the postmortem routine brain tissue samples. A list of test sample sources is presented in Table 1.

2.1.1 *Cryopreserved samples*

The native brain samples were incubated with Tissue-Tek O.C.T.™ Compound (Sakura®) (glycolen-based) and subsequently cooled and cut with a Cryostat (CM3050S, Leica Microsystems, Wetzlar, Germany). The cut brain slices were attached to coverslips (article number 1871, Carl Roth, Karlsruhe, Germany) and stored at −20°C. All brain tissues were cut orthogonally to the cortical layers.

2.1.2 *Paraffin-embedded samples*

For the fixation procedure (for samples fixed after 2007), the samples were incubated in a formalin solution for a period of ∼20 h (depending on sample size derived from the patient) and rinsed with distilled water. Thereafter, the samples were washed with a solution containing an ascending ethanol dilution series (60%, 70%, 80%, and 96% in distilled water and 100%; ∼10 h total wash time). Subsequently, the ethanol washing solution was replaced by xylol (99%, Dako, Vienna, Austria) for 1 h and embedded in paraffin for 30 min.

For the older fixation procedure (samples fixed before 2007), the timing for fixation steps with ethanol, xylol, and paraffin was different. After the biopsies, the samples were incubated in a formalin solution for a minimum of 4 h. The successive ascending ethanol dilution series (60%, 70%, 80%, and 96% in distilled water and 100%) were completed in 27 h. Thereafter, the ethanol was replaced with xylol (15 h) and embedded in paraffin for 12 h.

For both fixation methods, the paraffin-embedded samples were cut with a Mikrotom (RM2255, Leica) in ∼3-μm thick slices and attached to coverslips (the same as for the cryopreserved samples). To remove the paraffin, the samples were incubated with xylol and descending isopropanol series (96%, 80%, and 70% in distilled water). The epitope retrieval was conducted by boiling the sample in the washing solution (PT module, Thermo Scientific, Vienna, Austria) for 1 h. The samples were stored for maximum 7 days at room temperature (25°C) in Dulbecco's phosphate buffered saline (PBS) buffer until further usage.[23]

2.1.3 *Sample incubation*

To prepare the necessary reaction chamber, adhesive silicone isolators (JTR20-A-2.5, GRACE BIO-LABS, Oregon) were bound to the glass slide carrying the brain tissue. The samples

Table 1 Source of test—samples (Nerve Clinic Linz, Department of Pathology and Neuropathology)

Cryopreserved paraffin fixed		Sample group	Age	Cause of death	Gender	Diagnosis
C	Norm	A	67	Myocardial infarction	m	Normal, st.p. Astrocytoma
C	Norm	A	60	Incarceration, brain edema	f	Normal, edema
P	Norm	B	77	Cardial decompensation	f	Normal
P	Norm	B	75	Incarceration, brain bleeding	m	Normal
P_old	Norm	E	61	Cardial decompensation	m	Normal, st.p. Astrocytoma
P	Depr.	C	65	Myocardial infarction	m	Depression, alcoholism
P	Depr.	D	74	Myocardial infarction	f	Depression, Mb Alzheimer, Parkinson

were incubated for 12 h at 6°C with anti-GFAP, anti-HT_{1A}, and fetal calf serum as a competitor. After 12 h of incubation, the samples were rinsed once with Dulbecco's PBS buffer [1× (without Ca and Mg); PAA—The Cell Culture Company, Pasching, Austria]. To induce the Atto655 fluorophore blinking, cysteamine (2-mercaptoethylamine, Sigma Aldrich, Vienna, Austria) at a 20 to 40 mM concentration was used. All samples were measured within 24 h after incubation. All measurements were performed in Dulbecco's PBS buffer.

2.2 *Antibodies*

Astrocyte labeling: The astrocytes were marked with an anti-GFAP mouse anti-human monoclonal IgG antibody labeled with Alexa Fluor® 488 (Molecular Probes®, Vienna, Austria).

HT_{1A} receptor labeling: The HT_{1A} receptors were marked with an anti-HTR1A rabbit anti-human antibody (LS-B970/27181, Lifespan BioSciences Inc., Seattle) This antibody turned out to be best suited for immunohistochemistry experiments and is also used at the Nerve Clinic Linz (LNK) for neural standard screening.

Anti-HTR1A antibody was labeled via a N-hydroxysuccinimid (NHS)-ester bond with Atto655 (Attotec, Attotec. Labeling protocol, Siegen, Germany).

Seventy-five microliters of 1 mg/ml HTR1A (dissolved in PBS buffer and 2% sucrose) were diluted with a 0.2-M sodium bicarbonate buffer at a pH of 8.4. Thereafter, 1 μl of 0.25 mg/ml Atto655 dimethylsulfoxid (DMSO) solution was added to adjust a labeling ratio of ~1.8. The reaction mixture was incubated for 1 h at room temperature. To separate the labeled HTR1A antibodies from free dyes, a PD-10 Sephadex® G-25m column (GE Healthcare, Pittsburgh) was used. The labeling solution was purified via a PD-10 purification column in PBS buffer. To concentrate the labeled antibody, the eluate was pelleted (Thermo, Multifuge 1S-R, HERAEUS, Thermo Scientific, Vienna, Austria). The solution was split into three aliquots and stored at −20°C.

2.3 *Setup and Imaging*

The images were taken on a modified Olympus IX81 inverted microscope. The samples were illuminated through an Olympus UApo N 100×/1.49 NA oil objective with two diode lasers at 642-nm (Omicron Laserage Laserprodukte GmbH—Phoxx® 642, Rodgau-Dudenhofen, Germany) and 491-nm wavelength (Cobolt Calypso 100™, Solna, Sweden). The signal acquisition was carried out on an Andor iXonEM + 897 (back-illuminated) EMCCD (16-μm pixel size).

Used filter sets:

- Dichroic filter: FITC/Cy5 (ZT405/488/561/640rpc, Chroma, Olchin, Germay)
- Emission filter: FITC/Cy5 (446/523/600/677 nm BrightLine® quad-band bandpass filter, Semrock, Rochester)
- Additional emission filter: HQ 680/30 M (NC209774, Chroma, Olchin, Germay)

The experiments were performed using excitation powers of 3.35 and 0.025 kW/cm^2 at 642 and 491 nm, respectively. The samples were illuminated for 10 ms (642 nm) and 5 ms (491 nm) with 40 ms delay time. The illumination protocols were timed with a custom-made LabView®-based control software.

2.4 *Image Preprocessing*

The requirement of multicolor imaging presents additional challenges for tissue imaging and analysis. Given the low signal-to-noise ratio of single-molecule images, we have chosen a detection method based on the isotropic undecimated wavelet transform (IUWT).[24,25] Wavelet thresholding offers a robust solution for the detection of small bright features, for example, detection of subcellular structures labeled by fluorescent dyes. Since a fluorescent dye can be considered as a point light source, its image is the point-spread function of the optical system that can be approximated by a 2-D Gaussian shape. The typical noise model is photon count noise, following a Poisson distribution, and an additive Gaussian read-out noise:

$$n \sim \mathrm{Poi}(N) * \mathrm{Gauss}(0, \sigma),$$

with n is the number of detected photo-electrons, and N is the number of emitted photons.

For an EMCCD camera, the model including the effect of the multiplier can be approximated[26] by the equation:

$$p(n, N) \sim \mathrm{Gauss}\left[GN, FG\sqrt{(N)}\right] = \frac{1}{\sqrt{2\pi F^2 G^2 N}} \exp\left[\frac{-(n - GN)^2}{2F^2 G^2 N}\right],$$

where F represents the excess noise, and G is the average multiplier gain.

To deal with heterogeneity of the image noise, a variance-stabilizing transform is applied prior to the IUWT. The implementation of IUWT is based on the binomial filter $h = [1, 4, 6, 4, 1]/16$ as scaling function and the "à trous" algorithm.[25,27] The wavelet coefficients are computed as the difference between two successive scales. The wavelet coefficients of the finest resolution are discarded as noise. The remaining coefficients are threshold based on the control of false discovery rate as proposed in Ref. 28. The pixels considered significantly across scales are the result of the single-molecule detection step.

Subsequently, the detected molecules' position was determined with subpixel accuracy by least square fitting of a 2-D Gaussian function in the neighborhood of the detected significant pixels. An estimation of the localization accuracy was also calculated.[29,30]

2.5 *Single-Molecule Analysis*

Commonly, the position determination for image reconstruction is only limited by the single-molecule signal and the local background noise (see Thompson/Mortensen formula).[29,31] The fixation and epitope-retrieval protocols used guarantee good single-molecule detection. However, this assumption can be inaccurate, if, for example, the setup exhibits an intrinsic error in position determination. In order to consider this additional dynamic offset in the estimation of the position accuracy (PA), we assumed a bound fluorescent antibody as mobile and calculated the PA via error of the mean square displacement (MSD). The position deviation was described by MSD error estimation for a single trajectory using Qian formula[30,32,33]

$$\mathrm{var} = \frac{(4Dn\Delta T)^2(2n^2 + 1)}{3n(N - n - 1)},$$

where ΔT is the time delay between two frames, N is the number of steps in a trajectory, $n = t_{\mathrm{lag}}/\Delta T$ where t_{lag} is the sum of

illumination time and delay between the frames, and D is the diffusion constant.

In our approach, the calculated PA via MSD (offset of the MSD plot) is global (PA_g), averaged over all single-molecule signals detected over all frames, and describes the smallest localization radius in the image. To characterize the smallest possible localization accuracy of our setup, glass bound and sparsely distributed Atto655-labeled antibodies were used. The estimated PA was determined to be 22.2∓3.9 nm (approximately two to three times larger than the size of an antibody[34]). This value defines the resolution limit for the dSTORM images. Local position accuracies (PA_l) for individual single molecules were determined via standard deviation of the peak position over all illuminated frames within the maximal search radius of PA_g. For the image reconstruction, the mean values of all point coordinates detected within PA_g were used. In comparison, the calculated Thompson PA reaches a value of 11 nm (minimum); however, it does not take into account the setup properties.

2.6 *Image Sector Alignment*

Due to the heterogeneous laser profile and variations in setup adjustment in the particular experiments, the images analyzed at single molecule show a nonregular density profile along the y-axis (heterogeneous illumination). Therefore, for comparison of two sample images, it is necessary to choose the nearly homogenous illuminated sectors from both images. To ensure that both images have the same size, we first calculated the normalized molecule density distribution along the y-axis of an image. The normalized molecule density for a given y-value is the ratio of the density of molecules in an image segment with a length $[0, x_{max}]$ and a width $y \pm \Delta$ to the molecule density of the whole image (total number of molecules/image surfaces). The estimated density profile along the y-axis is then approximated with a one-dimensional Gauss function. The width of a segment is determined as width of the Gauss function at 50% of its maximal value (typically 140 to 200 pixels). An example of sector determination is presented in Fig. 1.

2.7 *Clustering-Based Spatial Analysis of Image*

In order to determine the spatial distribution pattern of receptors, we need to find characteristic parameters or image features, which will help us to quantify changes between the images. Classical spatial analysis uses the changes of selected spatial parameters, which take place when the distance scale (observation scale) is made to vary. The most popular method, proposed by Ripley (known as Ripley K- and L-functions),[35] describes the characteristics of the point groups (clusters) at many distance scales. For given maximal distance between points in cluster d, the Ripley's $L(d)$ function is estimated as

$$L(d) = \left[\lambda^{-1} \sum_i \sum_{j \neq i} k_{ij}(d_{ij} < d)/N\pi\right]^{1/2},$$

where Σk_{ij} is the summation over all points j that are within distance d of point i (including boundary condition), and λ is the density, which can be estimated as $\lambda = N/A$, where N is the observed total number of points, and A is the area of the analyzed sector. Although $L(d)$ can be determined for any d, it is common practice to consider d less than $\sim 1/3$, the shortest dimension of the studied area $\{d_{max} < \sim 1/3 \text{ min } [\text{size}(A)]\}$. Calculating $L(d)$ for $d = 1$ to d_{max} for the analyzed sector, we obtain the spatial pattern vectors L. This standard method for spatial analysis only examines the statistical density of all point clusters in the image sectors[35,36] and does not consider structural information such as the local density, shape of point clusters or relationships between clusters, and the structure of bulk fluorescence image. An example of Ripley's L-functions for two images is presented in Fig. 2.

Therefore, we propose a novel approach for spatial analysis based on clustering of preselected image sectors and cluster profiling. In our case, the Ripley's L-function is only used for establishing the significant interval of distance scale (cluster maximal size) d_{min} to d_{max} (Fig. 2).

The selected sector of points (single molecules) can be clustered in nonoverlapping clusters $C(d)$ with a cluster dimension less or equal to a given value $d[d \in (d_{min}, d_{max})]$. The dimension d of cluster (cluster size) is the maximal distance between points within the cluster. For fast clustering of a given sector of image, we use the hierarchical agglomerative clustering (HAC) method with complete link.[33] HAC clusters are established by cutting the dendrogram at a desired level so that each connected component (subclusters) forms a new cluster. The linkage between two clusters is achieved by complete linkage. This method is well suited for our consideration, because it takes into account the "similarity" between clusters based on the "outermost"

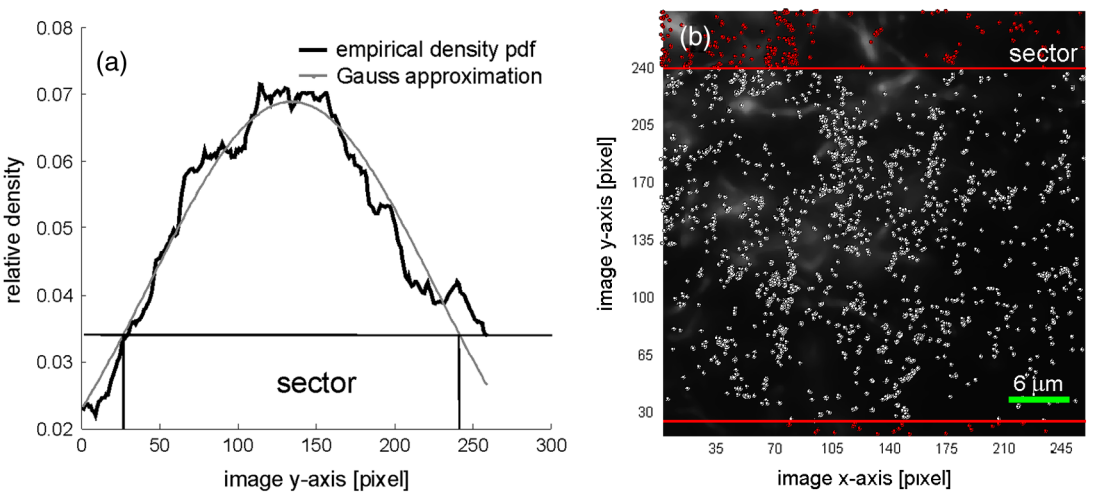

Fig. 1 (a) Empirical density distribution and a Gauss fit of molecule density along the y-axis of an image. (b) Selected sector of an image.

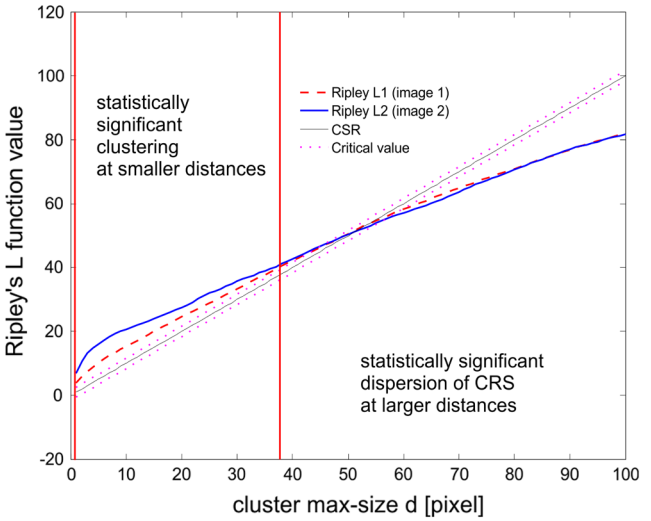

Fig. 2 Ripley's L-functions (distance d in pixel) for cryopreserved (L_1) and paraffin-fixed (L_2) images of a healthy brain tissue. Both samples show statistically significant clustering dissimilarity to complete spatial randomness (CSR) distribution at smaller distances and significant dispersion at larger distance. However, similarity between both samples (L_1 and L_2) is very high (p-value of Kolmogorov–Smirnov two-sample nonparametric test is equal to 0.96).

points [the least distance-similar (Ref. 33)] in clusters. The two clusters with a minimal complete linkage are merged in a new one. For a given distance d, HAC algorithm generates a lot of nonoverlapping clusters so that the dimension (size) of each cluster is less or equal d. The clusters represent stochastic distribution of points in selected sector, scaled into a cluster set. For each cluster, we defined local characteristics (features) which describe the spatial structure of a sector more accurately than with the standard spatial analysis method.

2.7.1 *Spatial properties of cluster*

Each cluster $c(d) \in C(d)$ can be characterized by the following local features:

1. Single fluorophore intensity determines the number of detected single fluorophores (or molecules). The cluster fluorophore ratio $\mathrm{fluor}[c(d)]$ is the proportion of fluorophore number per cluster to total number of fluorophores in the whole image sector. In an ideal case, where every antibody carries only one fluorophore and is imaged only once, the number of antibody-labeled receptors would be directly described by $\mathrm{fluor}[c(d)]$.

2. The relative density of cluster $\mathrm{dens}[c(d)]$ is the proportion of cluster density to the mean density of the complete image sector under consideration. The cluster density is determined as number of points (molecules) within a cluster per cluster area. The cluster area is calculated as the sum of the area inside the circle located at any point of the cluster with a radius equal to half the distance to its first nearest neighbor.

3. Cluster eccentricity: The best suited eccentricity definition for our analysis is based on central moments of points within a cluster.[35] As a measure of eccentricity, we took the proportion $\mathrm{ecc}[C(d)] = v_1/v_2$, where v_1 and v_2 are the eigenvalues of the symmetric 2×2 matrix M of central moments of cluster points. Such a measure is an invariant with respect to location, rotation, translation, and scaling of cluster. The eccentricity of a round-shaped cluster is equal to 1, and the eccentricity of a line-shaped cluster is equal to 0.

4. To determine the relationship between the cluster and the bulk fluorescent structure of the image, the skeleton representation of the bulk image sector is prepared.[37,38] The cluster distance-to-skeleton ratio $\mathrm{dist}[c(d)]$ is the proportion of the distance of the cluster centroid (mean position of points in the cluster) to the skeleton and of the mean distance of all points to the skeleton within an image sector. This representation of relationship between the clusters and the structure of the bulk fluorescent image enables additionally a more precise analysis of concentration and density of receptors surrounding, for example, glia structures.

An example of clustering and cluster features is presented in Fig. 3.

We gathered information about cluster properties in the aforementioned manner and compared the resulting data with cluster features extracted from randomly located points on the same image. The average eccentricity of the clusters changes from an almost circular shape to the shape of an elongated ellipse with increasing mean distance-to-skeleton and cluster size. A similar behavior was observed for changes in the density of the clusters. The average density of the cluster decreases with the increase of the average distance-to-skeleton and with the increase in the size of clusters. In contrast, the average eccentricity and average density of clusters for randomly located points is almost constant for all cluster sizes.

2.8 *Spatial Comparison of Image Sectors from Two Samples*

In order to characterize and compare the spatial distribution of single receptors between two image sectors of two samples, we applied the features described above for spatial analysis. For each cluster set, we used $C(d)$ derived from two sample images and computed the empirical feature distributions $\mathrm{fluor}(d)$, $\mathrm{dens}(d)$, $\mathrm{ecc}(d)$, and $\mathrm{dist}(d)$ for each distance d from the test interval $[d_{\min}, d_{\max}]$, respectively. Next, for a pair of such distributions (e.g., $\mathrm{dens}^1(d)$—first sample and $\mathrm{dens}^2(d)$—second sample) and for a d obtained from the clustering process of the first and second samples, we made two null hypotheses:

1. The null hypothesis I is that the empirical distributions of both samples are drawn from the same continuous distribution.

2. The null hypothesis II is that the first-sample empirical distribution cumulative distribution function (CDF) is larger than or equal to the second-sample empirical distribution CDF.

These distributions can be compared with the Kolmogorov–Smirnov two sample nonparametric test or with the Wilcoxon rank sum test.[39–41] We tested both hypotheses at the standard 5% significance level using a two-sample Kolmogorov–Smirnov

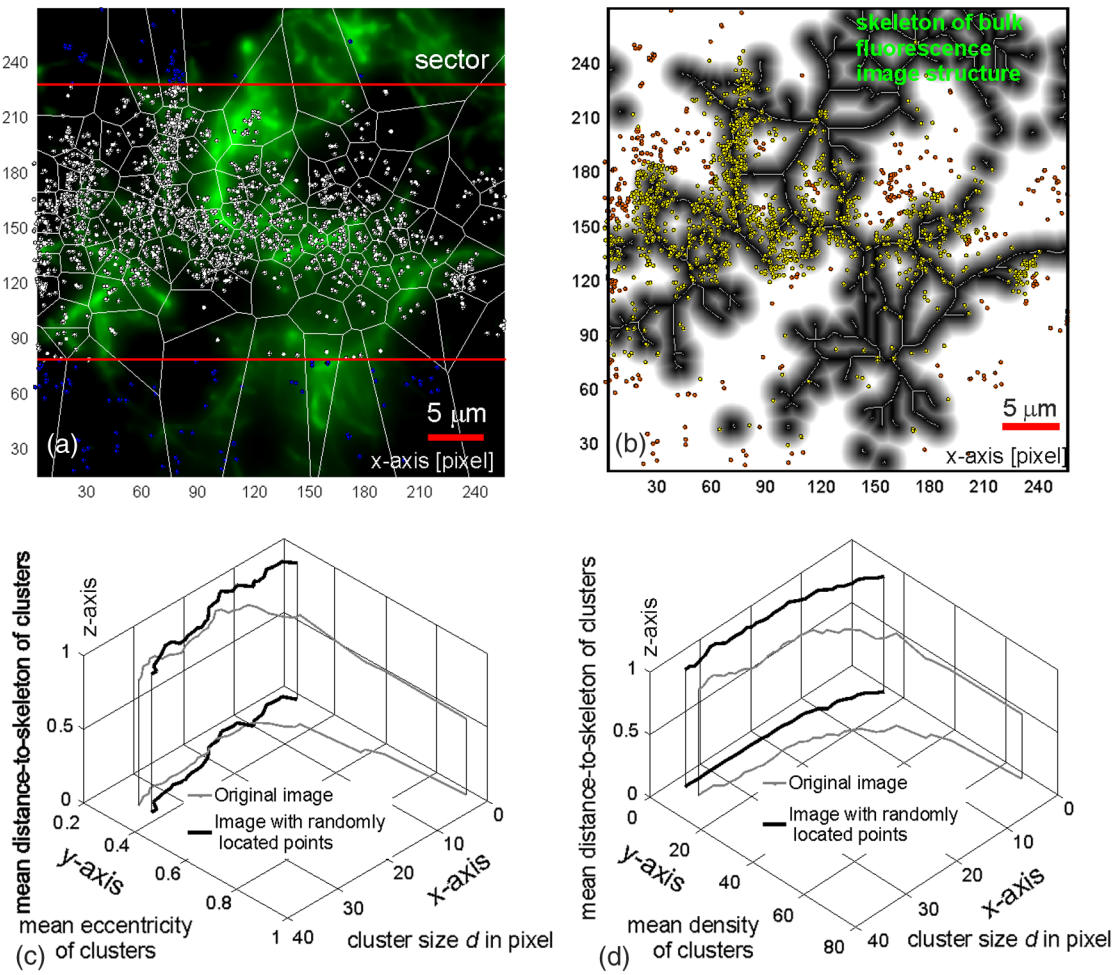

Fig. 3 Cluster and cluster features for cryopreserved sample images of a healthy brain tissue. (a) Image sector and clustering result for cluster max-size $d = 18$ pixels. (b) Skeleton of bulk fluorescence image (a) (glia tissue) and localized molecules (dots). (c) Mean value of clusters eccentricity (*y*-axis) and clusters distance-to-skeleton (*z*-axis) as function of cluster size (*x*-axis) for *d* from 1 to 35 pixels (light gray). For comparison, the clustering results for randomly located points on the same image are represented by the black. The eccentricity and distance-to-skeleton of randomly located points are almost constant for all cluster sizes. (d) Mean values of relative cluster density (*y*-axis) and cluster distance-to-skeleton (*z*-axis) as function of cluster size (*x*-axis) for *d* from 1 to 35 pixels (light gray). Black represents the same features for randomly located points. The mean density of cluster and mean distance-to-skeleton is almost constant, too.

test. The Kolmogorov–Smirnov test calculates the *p*-value $pv(d)$ between two empirical distributions for a given maximum size of clusters d. It is sensitive to differences between the empirical cumulative distribution functions of the two samples. The test rejects the null hypothesis (at the 5% significance level), if $pv(d) < 0.05$ [where $pv(d) = pv_{\text{equal}}(d)$ for test of hypothesis I and $pv(d) = pv_{\text{large}}(d)$ for test of hypothesis II]. Additionally, we apply a 2-D and two-sample Kolmogorov–Smirnov test.[42] This test compares a pair of 2-D distributions using Fasano and Franceschini's generalization of the Kolmogorov–Smirnov test.[42] The test of null hypothesis II can be applied to identify differences between samples, but only for selected spatial features of a cluster, for example the receptor–density distribution.

The test of null hypothesis I is used to define the similarity coefficient between two samples. The similarity coefficient is the mean of the weighted sum of the $pv(d)$ values for the different cluster features like fluor(d) and pairwise features like [dens(d), dist(d)] and [ecc(d), dist(d)] [throughout the range of cluster size (d)]. The weighted sum of the $pv(d)$ is called aggregated *p*-value $pv_{\text{agg}}(d)$.

$$pv_{\text{agg}}(d) = \sum \alpha_i pv_i(d)$$

$$\text{where } i \in \{\text{fluor}, (\text{dens} \times \text{dist}), (\text{ecc} \times \text{dist})\} \quad \text{and}$$

$$\sum \alpha_i = 1 \quad \text{similarity coefficient} = \text{Mean}_d[pv_{\text{agg}}(\text{d})].$$

To estimate the similarity or dissimilarity between two images, it is sufficient to compare these three *p*-values $pv(d)$ on the interval $[d_{\min}, d_{\max}]$. The analysis of the presented images by using the Ripley's L-function revealed an appearance of statistically significant clustering dissimilarity, when compared with a complete spatial randomness (CSR) distribution usually in the distance interval of $[d_{\min}, d_{\max}] = [1, \sim 35]$ pixels. This interval was chosen for the further estimation and comparison of pv_{large}-value functions. To exemplify the method described above, a comparison of two brain tissue images is presented in Fig. 4.

3 Results and Discussion

We analyzed dSTORM-imaged brain tissue samples with the presented method in order to extract cluster features of our

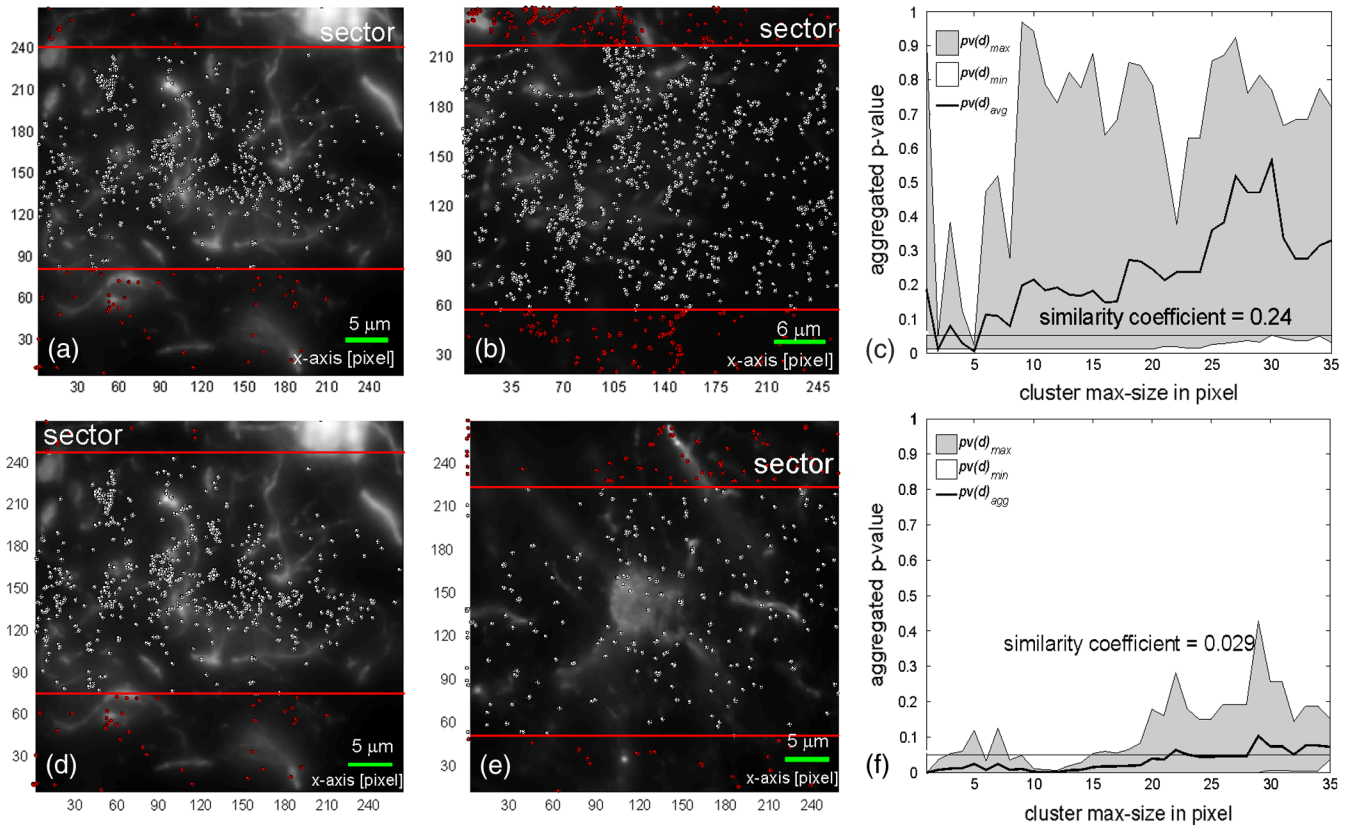

Fig. 4 (a) Image of a cryopreserved healthy brain tissue. (b) Image of a paraffin-fixed healthy brain tissue. (c) Comparison between (a) and (b) samples—$pv_{agg}(d)$ of cluster features distributions with similarity coefficient = 0.234 [gray zone shows minimal and maximal values of aggregated $pv(d)$]. (d) Image of a cryopreserved healthy brain tissue. (e) Image of a brain tissue of patient with depressive disease. (f) Comparison between (d) and (e) samples—$pv_{agg}(d)$ of cluster features distributions (similarity coefficient = 0.029).

protein of interest, the serotonin 5-HT_{1A} receptor. Since this receptor is expressed on the surface of neural as well as glial cells, we used the co-localization with an exclusively glial marker to demonstrate that this features-based analysis method is applicable for tissue classification at a nanoscopic level. To experimentally verify the presented method, neocortex tissue samples from healthy individuals and patients suffering from a mental disorder were used (see Table 1).

3.1 *STORM Imaging*

For dSTORM-imaging of serotonin receptor clusters on glial and nerve cells, the sample preparation methods and the illumination conditions had to be adapted. All measurements were performed on ~3-μm thin brain slices. To reduce autofluorescence and light scattering for two-color imaging, we used a total internal reflection fluorescence (TIRF) microscopy derived[43] highly inclined and laminated optical (HILO) sheet illumination configuration.[44,45] In this configuration, a laser beam is tilted through a single objective and leads to the illumination in only a thin intersection of the focal plane. The method is, however, not related to the wide-field imaging technique HiLo.[46,47]

The target proteins were labeled with commercially available antibodies marked with Alexa488 or Atto655 fluorophores (Attotec, Siegen, Germany). In case of the polyclonal anti-serotonin receptor antibody (Lifespan BioSciences Inc., Seattle), the labeling was performed via covalent amino fluorophore conjugation, and for the specific recognition of the glia, a monoclonal Alexa488-conjugated antibody (Molecular Probes, Vienna, Austria) against GFAP was used. We aimed to have a labeling ratio of 1.8 fluorophores per antibody, which guarantees that a relatively high amount of antibodies are labeled with just a single fluorophore and at the same time leads to a low abundance of blank antibodies. Due to this stochastic-labeling method, an exact quantification of the protein number within a serotonin receptor cluster is not possible. However, to guarantee the comparability of the samples measured in this work, all tissues are incubated with antibodies labeled in the same batch. Estimating more accurate numbers of serotonin receptors will require a labeling ration of one fluorophore per antibody and a detection system in which every fluorophore will only be imaged once. Moreover, the receptor recognition is also restricted to the binding affinity of the commercially available polyclonal antibodies. Due to their probabilistic binding kinetics, they cannot mark all successfully retrieved serotonin receptors.

We used the fluorescently labeled glia cells for orientation within the tissue slice by keeping the density of the glia cells in the imaged areas constant. Those receptor signals which did not colocalize with the glial skeleton are neural receptors and, interestingly, they also form clusters. However, only the anti-5HT_{1A} antibodies were characterized via localization microscopy. To apply dSTORM imaging, the photoswitching rate of Atto655 fluorophores needed to be adjusted to ensure sufficient long fluorophore off times. A 40 mM of cysteamin (MEA) were added to the measurement buffer. The Atto655-conjugated antibody was continuously illuminated at 4 mW/cm^2 power with a frame rate of 20 frames/s (~800 photons/fluorophore). Fast

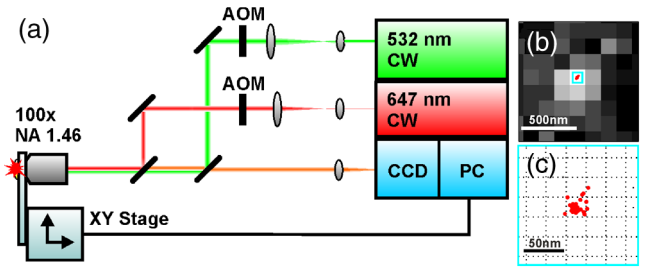

Fig. 5 (a) Single-molecule imaging setup. (b) Image of a single molecule with localized centers of all detected events from this molecule. (c) Zoom of the center pixel from (b).

illumination times and rather sparse serotonin clusters required 1200 frames for a fully reconstructed image. It was acquired within 1 min with localization accuracy down to 22.5 nm (Fig. 5). The described system adjustments are necessary to arrange two-color imaging and localization microscopy of fixed brain tissues (Fig. 6).

3.2 *Sample Comparison*

The presented image analysis was tested using samples from different patients (see Table 1), which were prepared following different fixation protocols. Generally, the test samples can be classified in the following groups: cryopreserved brain tissue of healthy individuals (Group A—13 samples), paraffin-fixed samples of healthy individuals (Group B—6 samples), samples taken from MDD patient with Alzheimer (Group C—2 samples), samples of a depressive (MDD) alcoholic patient (Group D—4 samples), and long-time preserved paraffin-fixed samples (Group E—3 samples).

We computed the aggregated $pv_{\mathrm{agg}}(d)$ functions for cluster size $d \in [d_{\min}, d_{\max}]$ and similarity coefficient for each pair of images within the same sample group and between different groups.

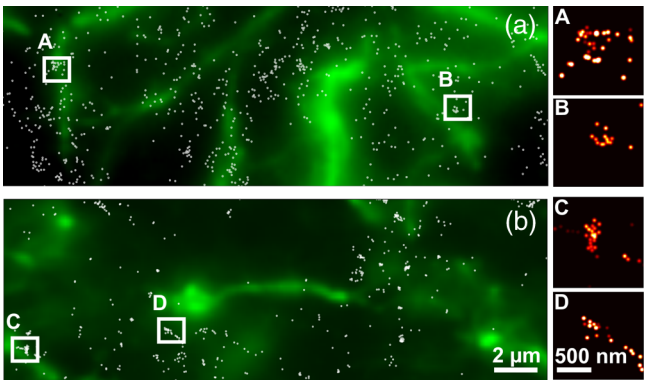

Fig. 6 (a) Image of the cryofixed brain tissue; green-labeled glia tissue with white-marked localized serotonin receptors (circle radius 27 ± 4.3 nm, pixel size 160 nm). The areas A and B represent zoomed out clusters of reconstructed images. In the reconstructed image, the localized single-molecule positions were fitted with a normalized Gauss, multiplied with maximal intensity of the dyes, and detected within PA_g (Gaussian FWHM = PA_g, pixel size 15 nm). (b) Image of the paraffin-fixed brain tissue (conserved in 2010; epitope retrieval 2012); green-labeled glia tissue with white-marked localized serotonin receptors (circle radius 28 ± 3.6 nm, pixel size 160 nm). The areas C and D represent zoomed out clusters of reconstructed images. All detected fluorophores were Gaussian fitted at their original positions (FWHM = PA_I, pixel size 15 nm).

Figure 7 presents the pairwise comparison matrix of images from all samples [Fig. 7(a)] and sample groups [Fig. 7(b)]. The grayscale (black—similarity coefficient = 1, white—similarity coefficient = 0) matrix elements represent the mean of the aggregated p-values, i.e., the pairwise similarity coefficient between the samples.

Based on this pairwise comparison, we constructed the global statistical similarity coefficient between the different sample groups. The global similarity coefficient between two groups of samples can be calculated as the mean value of similarity coefficients between all sample pairs from both groups.

3.3 *Spatial Cluster Analysis of Cryopreserved Samples (Group A)*

The first measurements were performed on cryopreserved samples. The cryogenic tissue preservation method was used for two reasons: first, to test the consistency of the brain slices, and second, to find a reference system for optimizing the fixation protocols for two-color imaging and for comparison with fixed healthy/pathologic tissue samples. Furthermore, the cryo-preservation method is also used to determine the antibody concentration required to saturate the serotonin H1 receptors in the brain tissue and to quantify the unspecific binding (incubation with unspecific Alexa647-labeled anti-GFP antibody). The concentration used was estimated to be 0.8 μg of antibodies per sample with almost 2 orders of magnitude higher specificity. The samples are derived from patients with no mental disability and died of cardiac decompensation and pulmonary edema with previous records of atrial fibrillation (see Table 1). The data were obtained from two patients with five and eight technical replicas, respectively [Fig. 7(a), submatrix A]. To ensure comparison between the same regions, only samples of the prefrontal cortex have been used. Moreover, we chose images with a similar density of the glia cells ($21 \pm 1.5\%$ average density), which was determined via intensity thresholding of the images' sectors, the same as used for cluster analysis. The threshold level was kept manually constant in all images. The comparison shows a 0.33 global similarity coefficient agreement between the cryopreserved samples. This result implies a good similarity between the samples regarding their cluster size, elliptic elongation, and density distribution in relation to the structure of the fluorescent bulk signal (glial tissue). Moreover, the results show that the proposed spatial analysis method is able to characterize serotonin H1 receptor clusters within human brain tissue at single-molecule level.

3.4 *Characterization of Fixation Artifacts (Groups B and E)*

The main objective of this study was to develop a method to quantify receptor distributions in thin sections of brain tissue on a nanoscopic level. Such a method should also be applicable to fixed samples stored for long periods. In a second step, we used the presented spatial analysis method to study the impact of the fixation method on sample quality. Therefore, we compared cryopreserved with paraffin-embedded tissues. The data of the paraffin-embedded tissue were collected from two patients [fixation year 2010 and three technical replicas for each patient—Fig. 7(a), submatrix B]. The analyzed images have a $20 \pm 3\%$ glia cell density. The comparison indicates a global similarity coefficient agreement of 0.2 inside the sample groups. Moreover, we also observed a high similarity between the

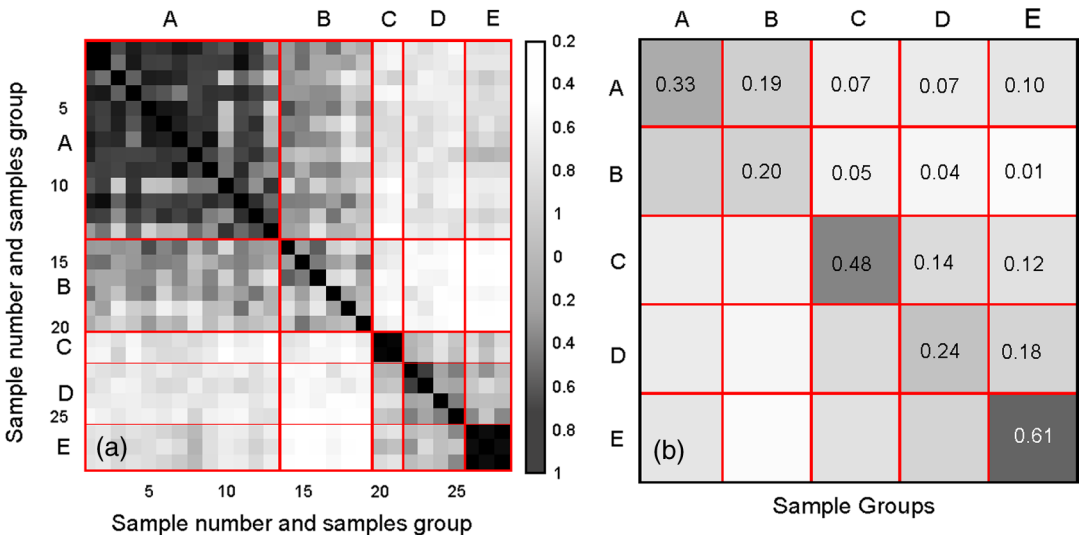

Fig. 7 (a) The similarity coefficient values between compared pairs of images from all sample groups (test of null hypothesis I). The submatrix A represents data from cryopreserved samples, submatrix B—paraffin-fixed samples prepared in 2010, submatrix C—a major depressive disorder (MDD) patient with Alzheimer as well as Parkinson, submatrix D—a depressive (MDD) alcoholic patient, and submatrix E—paraffin-fixed samples prepared 2007. A strong similarity between images from cryopreserved and paraffin-fixed samples (year 2010) is observed. Long-time preserved paraffin-fixed samples (year 2007) show much lower comparability to the earlier fixed and cryopreserved samples. Moreover, a strong dissimilarity between the cryopreserved and fixed samples versus patient group was observed. (b) Average of similarity coefficient values calculated between all samples groups—global similarity coefficient for null hypothesis I.

cryo- and paraffin-preserved tissues with global similarity coefficient of ∼0.2 between the samples. This confirms a good capability of our method for the comparison of tissue samples.

Furthermore, we wanted to test whether differences in the fixation protocols and extended storing times will have an impact on sample comparison. The comparability between differently treated and stored samples would significantly extend the applicability of the method [Fig. 7(a), submatrix E]. Paraffin samples had been prepared before 2007 by using a different fixation method and were compared with cryopreserved and freshly prepared paraffin samples. The comparison shows a global similarity of ∼0.1 to the cryopreserved tissue and a negligible similarity (global similarity of 0.018) to the paraffin-embedded slice. The data suggest that both the longer alcohol treatment in the older fixation procedure and the longer storage may have a negative impact on sample quality by causing a stronger epitope damage of the target protein. Consequently, for a precise comparison, our method requires consistency in sample conservation and fixation date as well.

3.5 *Spatial Cluster Analysis of Brain Tissue of Patients Suffering from a Mental Disorder (Groups C and D)*

To test the applicability of the localization microscopy and the cluster analysis in neuropathology, we concentrated on a very challenging field—the neuropathology of psychiatric disease. We compared healthy brain samples with samples of MDD patients (two patients with two and four technical replicas, respectively, each prepared in two individual batches). The first patient suffered from MDD and additionally from other diseases like Alzheimer's and Parkinson's (two technical replicas). The glia tissue density was shown to be around $19 \pm 0.5\%$ [Fig. 7(a), submatrix C]. This tissue displays a high 0.48 global similarity value for sample comparison inside the group. The second patient analyzed suffered from alcoholism; the four samples of this patient display a global similarity value of 0.24 at a glia tissue density of $20 \pm 3\%$ [Fig. 7(a), submatrix D]. We observed a dissimilarity between the brain tissues of the MDD patients and the healthy patient. We denote global similarity of 0.07 and 0.05 compared with healthy cryopreserved and paraffin-fixed tissues, respectively. The comparison between the two MDD patients displays a similarity coefficient value of ∼0.14, which shows a moderate agreement between the samples. These first results are promising for the future use of localization microscopy and the proposed special analysis technique for characterization and classification of human brain tissue. Although our study is limited to a small number of patients and to a single cortical region, the analysis reveals differences between pathological and healthy brain tissues which render the method applicable in the complex field of biological psychiatry.

3.6 *Relative Comparison of Cluster Features Between the Samples*

The presented method allows the classification of the samples based on their similarity; however, it does not provide statistical information about the relative cluster fluorophore number or density. Therefore, in a second comparison we determined the p_{larger}-value to test the null hypothesis II (for a definition see Sec. 2), which assumes that the first-sample empirical distribution CDF is larger than (or equal to) the second-sample empirical distribution CDF. A larger distribution corresponds to a larger cluster size and density by comparing one sample with the other. The comparison is restricted to individual features, for example, the relative number of fluorophores per cluster—fluor(d) or relative cluster density—dens(d). The test is performed within a cluster size interval of $d \in [1, 35]$ pixels. The result for relative cluster density distribution is presented in Fig. 8. The test of the null hypothesis II of cluster relative density was prepared on pairs of samples from groups A and B and samples from groups C and D.

The mean cluster density derived from C and D samples is smaller than from samples of healthy individuals (A and B

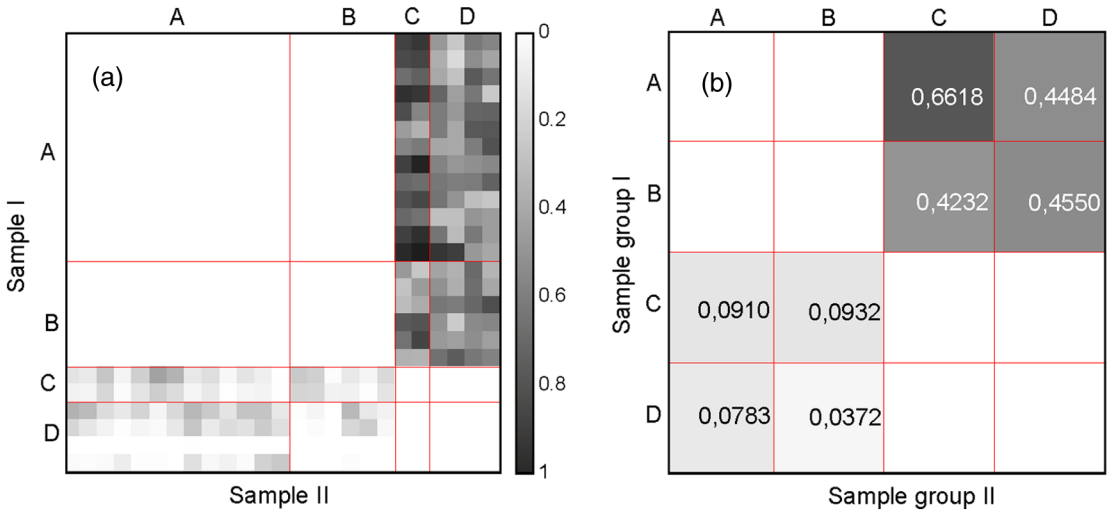

Fig. 8 (a) Mean p-value obtained from comparison between pairs of samples (over the complete distance interval) for testing of null hypothesis II [for dens(c[d])]: Group A—cryopreserved samples, group B—healthy paraffin-fixed samples, group C—first MDD patient, group D—second MDD patient. The distribution CDF of $\text{dens}_1(d)$ of sample 1 (rows) is larger than the distribution CDF of $\text{dens}_2(d)$ of sample 2 (columns). (b) Average pv_{large}-values between samples groups.

samples). Cryopreserved as well as paraffin-fixed samples of healthy individuals [Fig. 8(a), rows of submatrices A and B] show a high similarity between empirical CDFs of cluster density and fluorophore ratio with aggregated p_{larger}-values between 0.4 and 0.7 for cluster density and between 0.7 and 0.9 for cluster fluorophore ratio. In contrast, the samples from C and D groups [Fig. 8(a), rows of submatrices C and D] manifest a significantly lower similarity between CDFs of density and fluorophore ratio (aggregated p_{larger}-values between 0.04 and 0.09) compared with healthy brains samples from groups A and B.

4 Conclusions

Structural insights into receptor distribution within the brain have far-reaching consequences into the understanding of brain tissue composition and its changes due to mental illness and drug treatment. The analysis of small size clusters has up to now primarily relied on electron microscopy, which offers exquisite spatial resolution but has limitations in multicomponent analysis.[14,48] Fluorescence microscopy overcomes these limitations, but its diffraction limit does not allow exact position analysis of receptors.

Within this study, we successfully applied a dual-color, single-molecule, 2-D super-resolution method to determine the protein distribution of serotonin receptor 5-$\text{HT}_{1\text{AR}}$ in brain tissue. In particular, we were able to visualize serotonin receptor clusters at nanometer resolution level (down to 22.5 nm) in native and fixed dense light-scattering brain tissues. Our results were obtained from samples that are typically used in immunohistochemistry, which simplifies the implementation of our approach and shows a promising potential for more accurate analysis applications. The fast-imaging process further allows the recording of large sets of high-resolution images, which renders the comparative analysis between different tissue samples possible. The 2-D image of nanoscopically mapped serotonin receptors was used for a novel cluster-based analysis with respect to their sizes, densities, elongations, and relationship to bulk fluorescent structures (glia tissue). Herein, we would like to stress that the presented clustering method is the only technique which enables the combined analysis of localization microscopy and bulk fluorescence imaging. The proposed spatial analysis method allowed us to characterize the effects of long-term paraffin conservation and epitope retrieval on brain tissue. Also, the analysis method reveals differences between pathological (MDD) and healthy brain samples and indicates its potential application in tissue classification. In the case of 5-$\text{HT}_{1\text{AR}}$ receptors, which are expressed on glial as well as neural cells, the distribution of clusters is certainly influenced by several factors like, e.g., the cell type and cell-cell interactions or changes in pathological tissue morphology. Therefore, we applied correlative analysis between images of the glia tissue and single-molecule cluster distribution, which should include only the clusters associated with the labeled glial cells in the analysis.

Moreover, we would like to point out that the suggested clustering analysis method can also be adapted for three-dimensional analysis as well as for the characterization of any 2-D biological systems (e.g., Lat clustering on activated T-cell membranes).[49] The method also offers a more powerful alternative for the Ripley-K/L functions analysis method, which has limitations regarding the sample classification.

On the technical side, the presented work demonstrates that the combination of localization microscopy with a standard fixation method provides a powerful platform well suited for the analysis of biological tissue samples at a nanoscopic level. Our platform, therefore, marks a valuable technological advancement for the characterization of protein distributions in brain tissue.

Acknowledgments

The work described in this article was done within the research project Medical Proteomics Lab sponsored by Basic Research Program of the University of Applied Sciences Upper Austria. We would like to thank Nick Fulcher, Gregor Mendel Institute, Vienna for support and Mario Brameshuber, Institute of Applied Physics, Vienna University of Technology for providing us the anti-GFP antibody. Due to a tragic accident, Kurt Schilcher died shortly after the article was submitted. The work described in this article was done within the FIT-IT project number 835918 "NanoDetect: A

Bioinformatics Image Processing Framework for Automated Analysis of Cellular Macro and Nano Structures" sponsored by the Austrian Research Promotion Agency (FFG). This work was additionally supported by the Austrian Science Fund (FWF) (DK W1207; SFB 1710, 1711); the Austria Genomic Program (GENAU III); and the EU FP6 Programme Network of Excellence on Alternative Splicing (EURASNET) (LSHG-CT-2005-518238).

References

1. T. A. Klar and S. W. Hell, "Subdiffraction resolution in far-field fluorescence microscopy," *Opt. Lett.* **24**(14), 954–956 (1999).
2. T. A. Klar et al., "Fluorescence microscopy with diffraction resolution barrier broken by stimulated emission," *Proc. Natl. Acad. Sci. U. S. A.* **97**(15), 8206–8210 (2000).
3. S. W. Hell and J. Wichmann, "Breaking the diffraction resolution limit by stimulated emission: stimulated-emission-depletion fluorescence microscopy," *Opt. Lett.* **19**(11), 780–782 (1994).
4. M. G. Gustafsson, "Surpassing the lateral resolution limit by a factor of two using structured illumination microscopy," *J. Microsc.* **198**(2), 82–87 (2000).
5. L. Schermelleh et al., "Subdiffraction multicolor imaging of the nuclear periphery with 3D structured illumination microscopy," *Science* **320**(5881), 1332–1336 (2008).
6. E. Betzig, "Proposed method for molecular optical imaging," *Opt. Lett.* **20**(3), 237–239 (1995).
7. E. Betzig et al., "Imaging intracellular fluorescent proteins at nanometer resolution," *Science* **313**(5793), 1642–1645 (2006).
8. S. T. Hess, T. P. Girirajan, and M. D. Mason, "Ultra-high resolution imaging by fluorescence photoactivation localization microscopy," *Biophys. J.* **91**(11), 4258–4272 (2006).
9. M. J. Rust, M. Bates, and X. Zhuang, "Sub-diffraction-limit imaging by stochastic optical reconstruction microscopy (STORM)," *Nat. Methods* **3**(10), 793–795 (2006).
10. M. Heilemann et al., "Super-resolution imaging with small organic fluorophores," *Angew. Chem. Int. Ed. Engl.* **48**(37), 6903–6908 (2009).
11. S. van de Linde, M. Sauer, and M. Heilemann, "Subdiffraction-resolution fluorescence imaging of proteins in the mitochondrial inner membrane with photoswitchable fluorophores," *J. Struct. Biol.* **164**(3), 250–254 (2008).
12. H. Shroff et al., "Live-cell photoactivated localization microscopy of nanoscale adhesion dynamics," *Nat. Methods* **5**(5), 417–423 (2008).
13. H. Shroff, H. White, and E. Betzig, "Photoactivated localization microscopy (PALM) of adhesion complexes," *Curr. Protoc. Cell Biol.* Chapter 4 (Unit 4), 21 (2008).
14. A. Dani et al., "Superresolution imaging of chemical synapses in the brain," *Neuron* **68**(5), 843–856 (2010).
15. D. Baddeley et al., "4D super-resolution microscopy with conventional fluorophores and single wavelength excitation in optically thick cells and tissues," *PLoS One* **6**(5), e20645 (2011).
16. S. Nanguneri et al., "Three-dimensional, tomographic super-resolution fluorescence imaging of serially sectioned thick samples," *PLoS One* **7**(5), e38098 (2012).
17. M. Heilemann et al., "Carbocyanine dyes as efficient reversible single-molecule optical switch," *J. Am. Chem. Soc.* **127**(11), 3801–3806 (2005).
18. S. van de Linde et al., "Multicolor photoswitching microscopy for subdiffraction-resolution fluorescence imaging," *Photochem. Photobiol. Sci.* **8**(4), 465–469 (2009).
19. P. R. Albert and S. Lemonde, "5-HT_{1A} receptors, gene repression, and depression: guilt by association," *Neuroscientist* **10**(6), 575–593 (2004).
20. L. Christiansen et al., "Candidate gene polymorphisms in the serotonergic pathway: influence on depression symptomatology in an elderly population," *Biol. Psychiatry* **61**(2), 223–230 (2007).
21. D. Hoyer, J. P. Hannon, and G. R. Martin, "Molecular, pharmacological and functional diversity of 5-HT receptors," *Pharmacol. Biochem. Behav.* **71**(4), 533–554 (2002).
22. E. K. Lambe et al., "Serotonin receptor expression in human prefrontal cortex: balancing excitation and inhibition across postnatal development," *PLoS One* **6**(7), e22799 (2011).
23. Dako GmbH, *Education Guide: Immunohistochemical Staining Methods*, 4th ed., p. 183 (2006).
24. J. L. Starck, J. Fadili, and F. Murtagh, "The undecimated wavelet decomposition and its reconstruction," *IEEE Trans. Image Process.* **16**(2), 297–309 (2007).
25. J. C. Olivo-Marin, "Extraction of spots in biological images using multiscale products," *Pattern Recogn.* **35**(9), 1989–1996 (2002).
26. J. Hynecek and T. Nishiwaki, "Excess noise and other important characteristics of low light level imaging using charge multiplying CCDs," *IEEE Trans. Electron Dev.* **50**(1), 239–245 (2003).
27. L. Muresan et al., "Microarray analysis at single-molecule resolution," *IEEE Trans. Nanobiosci.* **9**(1), 51–58 (2010).
28. Y. H. Y. Benjamini, "Controlling the false discovery rate: a practical and powerful approach to multiple testing," *J. R. Stat. Soc.* **57**(1), 289–300 (1995).
29. R. E. Thompson, D. R. Larson, and W. W. Webb, "Precise nanometer localization analysis for individual fluorescent probes," *Biophys. J.* **82**(5), 2775–2783 (2002).
30. H. Qian, M. P. Sheetz, and E. L. Elson, "Single particle tracking. Analysis of diffusion and flow in two-dimensional systems," *Biophys. J.* **60**(4), 910–921 (1991).
31. K. I. Mortensen et al., "Optimized localization analysis for single-molecule tracking and super-resolution microscopy," *Nat. Methods* **7**(5), 377–381 (2010).
32. S. Wieser et al., "(Un)confined diffusion of CD59 in the plasma membrane determined by high-resolution single molecule microscopy," *Biophys. J.* **92**(10), 3719–3728 (2007).
33. S. Wieser and G. J. Schütz, "Tracking single molecules in the live cell plasma membrane-do's and don't's," *Methods* **46**(2), 131–140 (2008).
34. V. R. Sarma et al., "The three-dimensional structure at 6 A resolution of a human gamma Gl immunoglobulin molecule," *J. Biol. Chem.* **246**(11), 3753–3759 (1971).
35. P. M. Dixon, *Encyclopedia of Environmetrics*, John Wiley & Sons Ltd., Chichester, West Sussex, England (2006).
36. T. D. G. Shakhnarovich and P. Indyk, *Nearest-Neighbor Methods in Learning and Vision*, MIT Press, Cambridge, Massachusetts (2006).
37. P. Maragos and R. W. Schafer, "Morphological skeleton representation and coding of binary images," *IEEE Trans. Biomed. Eng. Acoustics, Speech Signal Process.* **34**(5), 1228–1244 (1986).
38. R. Kresch and D. Malah, "Skeleton-based morphological coding of binary images," *IEEE Trans. Image Process.* **7**(10), 1387–1399 (1998).
39. N. Smirnov, "On the estimation of the discrepancy between empirical curves of distribution for two independent samples," *Bull. Mathematique de l'Universite de Moscou* **2**, 3–16 (1939).
40. A. N. Kolmogorov, "On the empirical determination of a distribution function," *Giornale dell'Instituto Italiano degli Attuari* **4**, 83–91 (1933).
41. E. A. Gehan, "A generalized Wilcoxon test for comparing arbitrarily singly-censored samples," *Biometrika* **52**(1–2), 203–223 (1965).
42. R. Lopes, I. Reid, and P. Hobson, "The two-dimensional Kolmogorov-Smirnov test," in *XI Int. Workshop on Advanced Computing and Analysis Techniques in Physics Research*, Proc. Sci., Amsterdam, The Netherlands (2007).
43. D. Axelrod, "Cell-substrate contacts illuminated by total internal-reflection fluorescence," *Biophys. J.* **33**(2), A200 (1981)
44. M. Tokunaga, N. Imamoto, and K. Sakata-Sogawa, "Highly inclined thin illumination enables clear single-molecule imaging in cells," *Nat. Methods* **5**(2), 159–161 (2008).
45. J. Huisken and D. Y. Stainier, "Selective plane illumination microscopy techniques in developmental biology," *Development* **136**(12), 1963–1975 (2009).
46. J. Mertz et al., "Widefield fluorescence sectioning with HiLo microscopy," in *Conf. Proc. IEEE Eng. Med. Biol. Soc. 2009*, pp. 3229–3230 (2009).
47. D. Lim et al., "Optically sectioned in vivo imaging with speckle illumination HiLo microscopy," *J. Biomed. Opt.* **16**(1), 016014 (2011).
48. K. L. Briggman and W. Denk, "Towards neural circuit reconstruction with volume electron microscopy techniques," *Curr. Opin. Neurobiol.* **16**(5), 562–570 (2006).
49. D. J. Williamson et al., "Pre-existing clusters of the adaptor Lat do not participate in early T cell signaling events," *Nat. Immunol.* **12**(7), 655–662 (2011).